

Multi-mode Coherent Detection Ghost Imaging Lidar and Vibration-Mode Imaging

JINQUAN QI^{1,2}, SHUANG LIU¹, CHENJIN DENG^{1,*}, CHAORAN WANG^{1,2}, ZUNWANG BO¹, YOZHENG GUI^{1,2}, SHENSHENG HAN^{1,2,3,++}

¹*Wangzhijiang Innovation Center for Laser, Aerospace Laser Technology and System Department, Shanghai Institute of Optics and Fine Mechanics, Chinese Academy of Sciences, Shanghai 201800, China*

²*Center of Materials Science and Optoelectronics Engineering, University of Chinese Academy of Sciences, Beijing 100049, China*

³*Hangzhou Institute for Advanced Study, University of Chinese Academy of Sciences, Hangzhou 310024, Zhejiang, China*

^{*}dcj@siom.ac.cn

⁺⁺sshan@mail.shcnc.ac.cn

Abstract: Coherent detection ghost imaging lidar (CD-GI lidar) integrates ghost imaging with coherent detection, thereby achieving enhanced anti-interference and phase-resolved imaging capability. Here, we propose a bucket-detector-based multi-mode coherent detection scheme for CD-GI lidar, where the reflected multi-mode light fields are coherently mixed with a single-mode local oscillator (LO) at the bucket detector photosensitive plane. The bucket-detector-based multi-mode CD-GI lidar system breaks the constraints of Siegman antenna theorem by utilizing field correlation to decouple the reflected multi-mode light fields and reconstructs the spatial distribution of targets' vibration modes. Theoretical analysis of the bucket-detector-based multi-mode CD-GI lidar system is presented in this work, and its feasibility is verified through a series of experiments.

1. Introduction

Ghost imaging [1–3] has attracted significant interest in recent decades, as it can employ optical field fluctuation to encode and compress high-dimensional spatial image information into a lower-dimensional detection space that can be directly measurable by a detector, and allows the detection and imaging processes to be physically separated. Ghost imaging separates the tasks of optical signal acquisition and spatial resolution, enabling spatially resolved imaging performance comparable to that of detector arrays while operating within the spatiotemporal bandwidth product of a single detector. These advantages make it suitable for non-traditional imaging scenarios, including staring imaging radar [4–9], ultra-low dose X-ray imaging [10], electron [11], and neutron radiographic imaging [12, 13], as well as atomic ghost imaging [14], snapshot multidimensional ghost imaging [15, 16], super-resolution microscopic based on spectral ghost imaging [17], and scattering imaging [18–23], etc. Besides implementations based on intensity-correlations only can reconstruct the target's intensity image, subsequent developments in field correlation ghost imaging employing homodyne detection have shown that both quantum-entangled light sources [24] and classical thermal light sources [25] are capable of retrieving the complex reflectivity of the target.

With recent progress in optical coherent detection [26–29], it can now achieve sensitivity close to the shot-noise limit, just like intensity detection, and can effectively suppress background light interference while acquiring amplitude and phase information of the light field. These capabilities have motivated the development of coherent detection imaging lidar systems, notably: (i) synthetic aperture imaging lidar (SAIL), which achieves high spatial resolution through synthetic aperture synthesis [30–34], and (ii) coherent focal-plane array (FPA) imaging lidar, which enables real-time parallel detection with high detection efficiency [35–41]. However, the fundamental limitation of SAIL is that it relies on platform-induced relative motion to

modulate the return signal. Coherent FPA imaging, on the other hand, is challenged by the large spatiotemporal bandwidth product required for both detection and data processing [42, 43].

The integration of ghost imaging and coherent detection provides a promising alternative to the two previously mentioned coherent-detection-based imaging lidar systems [44, 45], which can retrieve spatial resolution by field correlation with the detected signal from single pixel point detector, relax the spatiotemporal bandwidth requirements on the receiver, and enable staring imaging without platform-induced relative motion. In this work, through theoretical analysis and experiments, we show that in the staring imaging mode, introducing bucket-detector-based multi-mode CD-GI lidar system breaks the constraint imposed by Siegman antenna theorem via field correlation to decouple the coherent summation of reflected multi-mode light fields and enables the simultaneous retrieval of both amplitude and phase information of the target, thereby achieving complex reflectivity imaging. Moreover, it allows access to the spatial distribution of targets' vibration modes in dynamic scenes within the field of view (FoV), thereby providing a approach for low spatiotemporal bandwidth product and staring imaging.

2. Method and Analysis

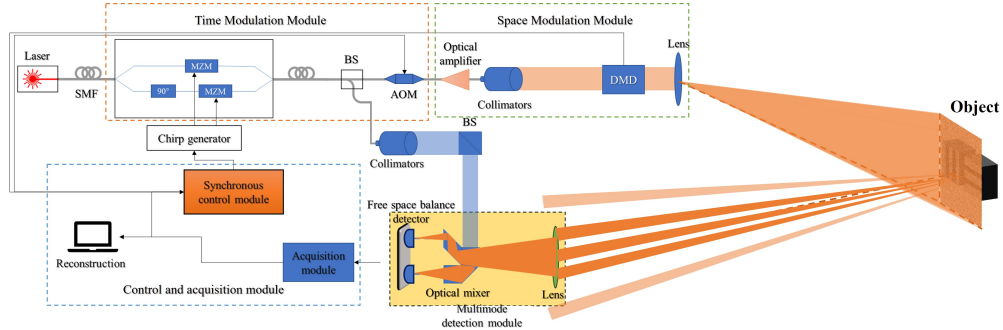


Fig. 1. Schematic of the bucket-detector-based multi-mode CD-GI lidar system.

Fig. 1 illustrates the bucket-detector-based multi-mode CD-GI lidar system. A spatiotemporally modulated laser field illuminates the target, and the resulting reflected multi-mode light fields are collected by a bucket detector and coherently mixed with a LO to produce an intermediate-frequency (IF) signal containing the target's amplitude and phase information.

2.1. Light field transmission and coherent detection

The spatiotemporally modulated light field is generated by the coordinated temporal and spatial modulation modules illustrated in Fig. 1. A narrow-linewidth laser serves as the seed source, whose emitted light field can be written as $E_0 = A_0 \exp(j2\pi f_c t)$, with a center frequency of f_c . To achieve distance resolution, the seed light is first modulated by an electro-optic modulator (EOM), which is driven by a chirped radio-frequency signal $s(t)$. The modulated beam is subsequently split by a fiber beam splitter into an object arm and a LO arm. In the object arm, an acousto-optic modulator (AOM) introduces a frequency shift f_{if} . Subsequently, the temporally modulated beam is collimated and incident onto a digital micromirror device (DMD) operating in an externally triggered mode synchronized with the temporal modulation period. The DMD is intrinsically a binary amplitude modulator, and generates a series of predefined spatial encoding patterns noted as $E_s^{(i)}(\rho_s) = A_s^{(i)}(\rho_s) \exp[j\phi_s^{(i)}(\rho_s)]$. Since the DMD is a pre-programmed encoding device acting only on the object arm, the reference-arm field can be expressed as a virtual encoding: $E_r^{(i)}(\rho_r) = A_s^{(i)}(\rho_r) \exp[j\phi_s^{(i)}(\rho_r)]$. This process generates

a spatiotemporally modulated transmitted field, which can be represented as:

$$E_{\text{Sig}}^{(i)}(\rho_s, t) = \sqrt{\eta_{\text{Sig}}} A_0 \cdot \exp[j2\pi(f_c + f_{if})t] \cdot s(t) \cdot E_s^{(i)}(\rho_s), \quad (1)$$

and a LO field:

$$E_{\text{Lo-mod}}(t) = \sqrt{\eta_{\text{Lo}}} A_0 \cdot \exp(j2\pi f_c t) \cdot s(t), \quad (2)$$

where i denotes the i -th pulse, $\eta_{\text{Sig}} \approx 0.99$ and $\eta_{\text{Lo}} \approx 0.01$ denote the power splitting ratios.

After propagation through a imaging transmitting system, as shown in Fig. 1, the modulated field illuminates the target, which is modeled by a spatially varying complex reflectivity combined with a time-dependent phase term accounting for range variations or surface vibrations:

$$\tilde{T}(\rho_o, t) = t_o(\rho_o) \exp[j\phi_o(\rho_o)] \cdot \exp[j2kz(\rho_o, t)], \quad (3)$$

where $t_o(\rho_o)$ indicates the amplitude reflectivity of target, $\phi_o(\rho_o)$ represents the phase of target and $z(\rho_o, t)$ indicates the distance variation caused by the micro-vibration of target. The resulting multi-mode back-scattered field is collected by the imaging receiving system and coherently interfered with the LO in a spatial optical mixer, followed by the balanced bucket detector. The architecture of this multi-mode detection module is described in Fig. 1.

The reflected light fields on the surface of the detector can be represented as (see Supplement 1, Sec. S1 for detailed derivation process):

$$\begin{aligned} E_d^{(i)}(\rho_d, t) = & \frac{\exp[jk(z_1 + z_2 + z_3 + z_4)]}{\lambda^4 z_1 z_2 z_3 z_4} \exp\left[\frac{j\pi}{\lambda z_4} |\rho_d|^2\right] s(t - \tau) \cdot \exp[j(\phi_{i,1} + \phi_{i,2})] \\ & \times \int_{A_o} \exp\left[\frac{j\pi}{\lambda} \left(\frac{z_1 + z_2}{z_2^2} + \frac{1}{z_3}\right) |\rho_o|^2\right] E_s^{(i)}\left(-\frac{z_1}{z_2} \rho_o\right) \tilde{T}(\rho_o, t) \frac{J_1\left(\frac{D_f \pi}{\lambda} \left(\frac{\rho_o}{z_3} + \frac{\rho_d}{z_4}\right)\right)}{\frac{\pi}{\lambda} \left(\frac{\rho_o}{z_3} + \frac{\rho_d}{z_4}\right)} d\rho_o \end{aligned} \quad (4)$$

where $k = 2\pi/\lambda$ represents the wave number; z_1 and z_2 denote the object distance and image distance of the imaging transmitting system; z_3 and z_4 denote the object and image distances of the reception imaging system; $\exp[j(\phi_{i,1} + \phi_{i,2})]$ represents the overall phase distortion introduced by atmospheric turbulence during the propagation of the i -th spatial modulated pattern, $\phi_{i,1}$ and $\phi_{i,2}$ represent the turbulence-induced phase perturbations along the forward and return propagation paths; D_f represents the aperture diameter of the receiving lens; A_o represents the target area; $\rho_o = (x_o, y_o)$ denotes the transverse coordinates on the target plane and $\rho_d = (x_d, y_d)$ denotes the transverse coordinates on the detector plane. After balanced detection, the optical signal is converted into an electrical signal $i^{(i)}(t)$:

$$\begin{aligned} i^{(i)}(t) &= \frac{1}{2} R \cdot \int_{A_d} \left[E_d^{(i)}(\rho_d, t) E_{\text{Lo-mod}}^*(t) + \text{c.c.} \right] d\rho_d \\ &= R \cdot \int_{A_d} \int_{A_o} A_1(\rho_o, \rho_d) \cos[\phi(\rho_o, \rho_d, t)] d\rho_o d\rho_d. \end{aligned} \quad (5)$$

$$A_1(\rho_o, \rho_d) = \frac{\sqrt{\eta_{\text{Sig}}} \sqrt{\eta_{\text{Lo}}}}{\lambda^4 z_1 z_2 z_3 z_4} A_s^{(i)}\left(-\frac{z_1}{z_2} \rho_o\right) A_0^2 t_o(\rho_o) \cdot \frac{J_1\left(\frac{D_f \pi}{\lambda} \left(\frac{\rho_o}{z_3} + \frac{\rho_d}{z_4}\right)\right)}{\frac{\pi}{\lambda} \left(\frac{\rho_o}{z_3} + \frac{\rho_d}{z_4}\right)} \quad (5.1)$$

$$\begin{aligned} \phi(\rho_o, \rho_d, t) &= k(z_1 + z_2 + z_3 + z_4) + \frac{\pi}{\lambda z_4} |\rho_d|^2 + \phi_o(\rho_o) + \phi_s^{(i)}\left(-\frac{z_1}{z_2} \rho_o\right) + 2\pi f_{if} t \\ &+ \frac{\pi}{\lambda} \left(\frac{z_1 + z_2}{z_2^2} + \frac{1}{z_3}\right) |\rho_o|^2 + 2\pi \left(\frac{B}{T} \tau t + f_0 \tau - \frac{B}{2T} \tau^2\right) + 2kz(\rho_o, t) + \phi_{i,1} + \phi_{i,2} \end{aligned} \quad (5.2)$$

Here, $\tau = (z_1 + z_2 + z_3 + z_4)/c$ is the time delay caused by the target distance; R denotes the responsivity of the detector; *c.c.* denotes the complex conjugate of $E_d^{(i)}(\rho_d, t)E_{\text{Lo-mod}}^*(t)$ and A_d represents the area of the detector.

2.2. Signal processing and Vibration-Mode imaging reconstruction

A static target can be regarded as a target with vibration frequency of zero. To obtain an explicit expression for the IF signal, the Fast Fourier transform is applied to $i^{(i)}(t)$ (L is the total length of the signal.), yielding (see Supplement 1, Sec. S2 for detailed derivation process):

$$\begin{aligned} \widetilde{i^{(i)}} \left(f = f_{if} + \frac{B}{T} \tau \right) &= \frac{L}{2} A_0^2 \pi R \frac{\sqrt{\eta_{\text{Sig}}} \sqrt{\eta_{\text{Lo}}}}{\lambda^4 z_1 z_2 z_3 z_4} \exp \left[jk(z_1 + z_2 + z_3 + z_4) + j2\pi \left(f_0 \tau - \frac{B}{2T} \tau^2 \right) \right] \\ &\quad \times \int_{A_d} \exp \left(\frac{j\pi}{\lambda z_4} |\rho_d|^2 \right) \int_{A_o} \exp \left[\frac{j\pi}{\lambda} \left(\frac{z_1 + z_2}{z_2^2} + \frac{1}{z_3} \right) |\rho_o|^2 \right] \\ &\quad \times \frac{J_1 \left[\frac{D_f \pi}{\lambda} \left(\frac{\rho_o}{z_3} + \frac{\rho_d}{z_4} \right) \right]}{\frac{\pi}{\lambda} \left(\frac{\rho_o}{z_3} + \frac{\rho_d}{z_4} \right)} E_s^{(i)} \left(-\frac{z_1}{z_2} \rho_o \right) \tilde{T}(\rho_o) d\rho_o d\rho_d \cdot \exp(j\phi_i), \end{aligned} \quad (6)$$

where $\phi_i = \phi_{i,1} + \phi_{i,2}$. Due to the phase disturbances arising during the detection process, an appropriate phase correction is required to recover the IF signal:

$$\widetilde{i}_{\text{correct}}^{(i)} \left(f = f_{if} + \frac{B}{T} \tau \right) = \frac{L}{2} A_0^2 \pi R \frac{\sqrt{\eta_{\text{Sig}}} \sqrt{\eta_{\text{Lo}}}}{\lambda^4 z_1 z_2 z_3 z_4} \cdot \frac{\int_{A_o} W(\rho_o) E_s^{(i)} \left(-\frac{z_1}{z_2} \rho_o \right) \tilde{T}(\rho_o) d\rho_o}{\exp \left[j \cdot \arg \left(\int_{A_o} W(\rho_o) \tilde{T}(\rho_o) d\rho_o \right) \right]}, \quad (7)$$

$$W(\rho_o) = \exp \left[\frac{j\pi}{\lambda} \left(\frac{z_1 + z_2}{z_2^2} + \frac{1}{z_3} \right) |\rho_o|^2 \right] C(\rho_o), \quad (7.1)$$

$$C(\rho_o) = \int_{A_d} \exp \left(\frac{j\pi}{\lambda z_4} |\rho_d|^2 \right) \frac{J_1 \left[\frac{D_f \pi}{\lambda} \left(\frac{\rho_o}{z_3} + \frac{\rho_d}{z_4} \right) \right]}{\frac{\pi}{\lambda} \left(\frac{\rho_o}{z_3} + \frac{\rho_d}{z_4} \right)} d\rho_d, \quad (7.2)$$

where $(i) \in \mathbb{N}$ and $\arg(\cdot)$ denotes extracting the phase of a complex signal. The correction procedure, the detailed derivation of the corrected IF signal and the field correlation image of the complex reflectivity for a static target are provided in Supplement 1, Sec. S2.A.

In practical remote-sensing scenarios, many targets exhibit micro-vibration motions, such as engine-induced vibrations [46], rotor oscillations [47], and structural flutter [48], which arise from continuous external excitation and manifest as steady-state periodic displacements. In this work, the target is assumed to undergo continuous vibration throughout the sampling interval.

Without loss of generality, an arbitrary vibration can be decomposed into a superposition of sinusoidal components [49]. Consequently, we adopt a canonical sinusoidal vibration model along the axial direction:

$$z(\rho_o, t) = \Delta z(\rho_o) \sin [2\pi f_v t + \varphi_o(\rho_o)], \quad (8)$$

where $\Delta z(\rho_o)$ is the vibration amplitude, f_v is the vibration frequency and $\varphi_o(\rho_o)$ is the initial vibration phase.

Since the experimental system can extract the target's time frequency information from the Short-time Fourier transform (STFT) spectrum [50–53]. To ensure that the spatiotemporal modulation on the DMD is synchronized with the target vibration, the repetition rate of the spatial modulation sequence on the DMD is set to be an integer divisor of the vibration frequency. Under this condition, assuming the total length of the signal $i^{(i)}(t)$ is L , a sliding rectangular window function $w(t)$ is used with length l and overlap d , k is the number of the corresponding windows: $k = 0, 1, 2, \dots, \lfloor \frac{L-l}{l-d} \rfloor$. After performing field correlation of the corrected complex signal $\tilde{i}_{\text{correct}-k}^{(i)} \left(f = \omega_k^{(h)} / 2\pi \right)$, which corresponds to the h -th micro-Doppler frequency in the k -th time slice of the STFT spectrum, with the reference-arm field $\left[E_r^{(i)}(\rho_r) \right]^*$, we can obtain the spatial distribution corresponding to the micro-Doppler frequency for $f = \omega_k^{(h)} / 2\pi$ of the target:

$$\begin{aligned}
G_k^{(h)}(\rho_r) &= \left\langle \tilde{i}_{\text{correct}-k}^{(i)} \left(f = \frac{\omega_k^{(h)}}{2\pi} \right) \cdot \left[E_r^{(i)}(\rho_r) \right]^* \right\rangle_i \\
&\propto A_0^2 \pi l R \frac{\sqrt{\eta_{\text{Sig}}} \sqrt{\eta_{\text{Lo}}}}{\lambda^4 z_1 z_2 z_3 z_4} \exp \left[jk(z_1 + z_2 + z_3 + z_4) - j\omega_k^{(h)} \left[k(l-d) + \frac{l}{2} \right] \right] \text{sinc} \left(\frac{\omega_k^{(h)} l}{2} \right) \\
&\times \exp \left[j2\pi \left(f_0 \tau - \frac{B}{2T} \tau^2 \right) \right] \exp \left[\frac{j\pi}{\lambda} \left(\frac{z_1 + z_2}{z_2^2} + \frac{1}{z_3} \right) \left| -\frac{z_2}{z_1} \rho_r \right|^2 \right] \frac{J_1 \left[\frac{D_f \pi}{\lambda} \left(\frac{z_2}{z_1 z_3} \rho_r \right) \right]}{\frac{\pi}{\lambda} \left(\frac{z_2}{z_1 z_3} \rho_r \right)} \\
&\times \tilde{T}_k^{(h)} \left(-\frac{z_2}{z_1} \rho_r \right).
\end{aligned} \tag{9}$$

Here, the ensemble averaging $\langle \cdot \rangle$ is performed over the encoded optical field i corresponding to the h -th micro-Doppler frequency component within the k -th time window. The vibration amplitude corresponding to the target spatial position can be converted as follows (see Supplement 1, Sec. S2.B for detailed derivation process):

$$A_k^{(h)}(\rho_r) = \frac{\left[\frac{\omega_k^{(h)}}{2\pi} - f_{if} - \frac{B}{T} \tau \right] \lambda}{4\pi f_v}. \tag{10}$$

Field correlation reconstruction is sequentially performed over the k time windows defined by the STFT. The spatial images reconstructed from these windows are combined with the corresponding vibration amplitude to recover the target's vibration modes.

2.3. Analysis

The previous section presents a comprehensive analytical framework for the bucket-detector-based multi-mode CD-GI lidar system. In the following, we proceed with a detailed analysis.

The imaging receiving module employed in this work constitutes a imaging system, as described in Eq. (4). Under the paraxial approximation and a fixed receiving optical configuration, the maximum angular FoV satisfies $\theta_{\text{FoV}} \approx D_{\text{det}}/f$, where D_{det} denotes the effective detector width and f is the focal length of the receiving lens. Accordingly, the FoV on the target plane scales linearly with the detector size and can be expressed as $\text{FoV} \approx \theta_{\text{FoV}} \cdot z_3 \approx D_{\text{det}} \cdot M$, where $M = z_3/z_4$ denotes the magnification of the imaging receiving module. Therefore, under the assumption of an unbounded image-side FoV, for a fixed receiving optical system, enlarging the detector directly expands the accessible imaging area on the target plane.

2.3.1. Analysis for the IF signal energy of reflected light fields

Under the paraxial approximation, the IF signal in Eq. (6) can be reformulated in the wave-vector domain by expressing both the reflected multi-mode light fields and LO fields using angular spectrum representation [54, 55] and integrating over the finite detector area. The detailed derivation is provided in Supplement 1, Sec. S3.A. The resulting expression can be written as:

$$\begin{aligned} \tilde{t}^{(i)}(f = f_{if}) = & R\sqrt{\eta_{\text{Sig}}}\sqrt{\eta_{\text{Lo}}}A_0^2 \frac{\exp[jk(z_1 + z_2 + z_3 + z_4)]}{\lambda^4 z_1 z_2 z_3 z_4} \\ & \times \int_{|\kappa|} \int_{A_o} \exp\left[\frac{j\pi}{\lambda} \left(\frac{z_1 + z_2}{z_2^2} + \frac{1}{z_3}\right) |\rho_o|^2\right] E_s^{(i)}\left(-\frac{z_1}{z_2} \rho_o\right) \tilde{T}(\rho_o) \exp\left[-j2\pi \frac{z_4}{z_3} \rho_o \kappa\right] d\rho_o \\ & \times \prod \left(\frac{|\kappa|}{\kappa_c}\right) \exp[j\pi\lambda z_4 |\kappa|^2] \pi\left(\frac{D_{\text{det}}}{2}\right)^2 \frac{2J_1\left(\frac{D_{\text{det}}}{2} |\kappa - \kappa_{\text{lo}}|\right)}{\frac{D_{\text{det}}}{2} |\kappa - \kappa_{\text{lo}}|} d\kappa, \end{aligned} \quad (11)$$

where $\kappa_c = \frac{D_f}{\lambda z_4}$ is the receiving system cutoff spatial frequency, κ_{lo} denotes the transverse wave vector (angular spectrum component) of the single-mode LO and D_{det} is the diameter of bucket detector. This integral expression with κ explicitly shows that the detector area imposes a spatial-frequency weighting on the IF signal, thereby determining whether the detection process operates in the single-mode or the multi-mode regime.

1. **Single-mode light field:** When the detector diameter D_{det} is smaller than the effective Airy disk corresponding to the receiving aperture, the detector can be approximated as a point detector, yielding $D_{\text{det}} \leq 2\lambda z_4/D_f$. In this case, the detected field can be regarded as single-mode. As the detector size continues to increase, the IF signal energy exhibits a tendency toward stable oscillations, as dictated by the integral properties of the Bessel function and consistent with the Siegman antenna theorem [56].
2. **Multi-mode light field:** When the detector diameter exceeds the Airy disk $D_{\text{det}} > 2\lambda z_4/D_f$, the detector behaves as a bucket detector that integrates multiple spatial modes over its active area. In this regime, the detected reflected light fields must be treated as multi-mode. With further increase in detector size, the integration includes multiple single-mode fields, and the IF signal energy statistically converges to a stable oscillatory regime as described by Siegman antenna theorem [56].

In summary, the coherent detection performance is governed by the spatial-mode matching between the reflected light fields and LO fields, together with the detector's effective area, as described by Siegman antenna theorem. A small detector favors single-mode detection, whereas increasing the detector size enables the collection of multiple spatial modes. In the presence of reflected multi-mode light fields, the IF signal energy rises to saturation and then oscillates as described in Siegman antenna theorem.

2.3.2. Analysis for the energy of field correlation image

The field correlation can be expressed in the wave-vector domain as:

$$\begin{aligned} G[\rho_r^{(m,n)}] \propto & \sum_{m,n} \left\{ \tilde{t}_o(\alpha \kappa_{m,n}) * \left[\text{sinc}(\beta \kappa_{m,n}) e^{j2\pi\gamma \rho_r^{(m,n)} \kappa_{m,n}} \right] \right\} \\ & \times \Delta\kappa^2 \prod \left(\frac{|\kappa_{m,n}|}{\kappa_c}\right) \pi\left(\frac{D_{\text{det}}}{2}\right)^2 \frac{2J_1\left(\frac{D_{\text{det}}}{2} |\kappa_{m,n} - \kappa_{\text{lo}}|\right)}{\frac{D_{\text{det}}}{2} |\kappa_{m,n} - \kappa_{\text{lo}}|}, \end{aligned} \quad (12)$$

$$\alpha = \frac{z_4}{z_3}, \beta = \frac{z_4 z_2}{z_3 z_1}, \gamma = \frac{z_4}{z_3 z_1}, \tilde{t}_o(\alpha \kappa) = \mathcal{F}\{\tilde{t}(\rho_o)\}, \quad (12.1)$$

where $\tilde{t}(\rho_o) = \exp \left[\frac{j\pi}{\lambda z_2} |\rho_o|^2 + \frac{j\pi z_1}{\lambda z_2^2} |\rho_o|^2 + \frac{j\pi}{\lambda z_3} |\rho_o|^2 \right] \tilde{t}(\rho_o)$ denotes the effective target response, defined as the product of the target's complex reflectivity and the quadratic phase factor introduced by free-space propagation, $\rho_r^{(m,n)}$ indicates the discretized reference arm coordinates at the index (m, n) and $\kappa_{m,n}$ denotes the discretized wave vector at the index (m, n) . The detailed derivation is provided in Supplement 1, Sec. S3.B.

Assuming the minimum feature size of the pattern $E_s^{(i)}(\rho_r)$ is d_{pixel} (e.g., the smallest unit in Hadamard or binary coding), then under far-field conditions, each minimum pattern unit corresponds to an angular spectrum component satisfying: $\kappa_{m,n} \sim z_4/(z_3 d_{\text{pixel}}^{(m,n)})$.

As can be seen from Eqs.(11) and (12), although the IF signal energy of the bucket-detector-based multi-mode CD-GI lidar is constrained by Siegman antenna theorem, by exploiting field correlation, it is able to decouple the reflected multi-mode light fields collected by the bucket detector into effective single-mode components determined by the pixel size, thereby circumventing the constraint imposed by Siegman antenna theorem. In addition, imaging can be achieved using a single bucket detector with a spatiotemporal bandwidth product that is reduced compared with that required by a coherent focal-plane array imaging lidar under the same conditions.

3. Experiment

The experimental system for the bucket-detector-based multi-mode CD-GI lidar is illustrated in Fig. 2. A narrow-linewidth continuous-wave seed source with a central wavelength of 1550 nm (Shanghai Precilasers Technologies Co. Ltd., FL-SF-1550-S) is transmitted via a single-mode optical fiber to a IQ modulator (MXIQUER-LN-30, iXblue). The chirped RF signal driving the modulator is generated by a direct digital synthesizer (Analog Devices Inc., AD9914). The modulation signal has a bandwidth of 800 MHz and a modulation period of 1 ms.

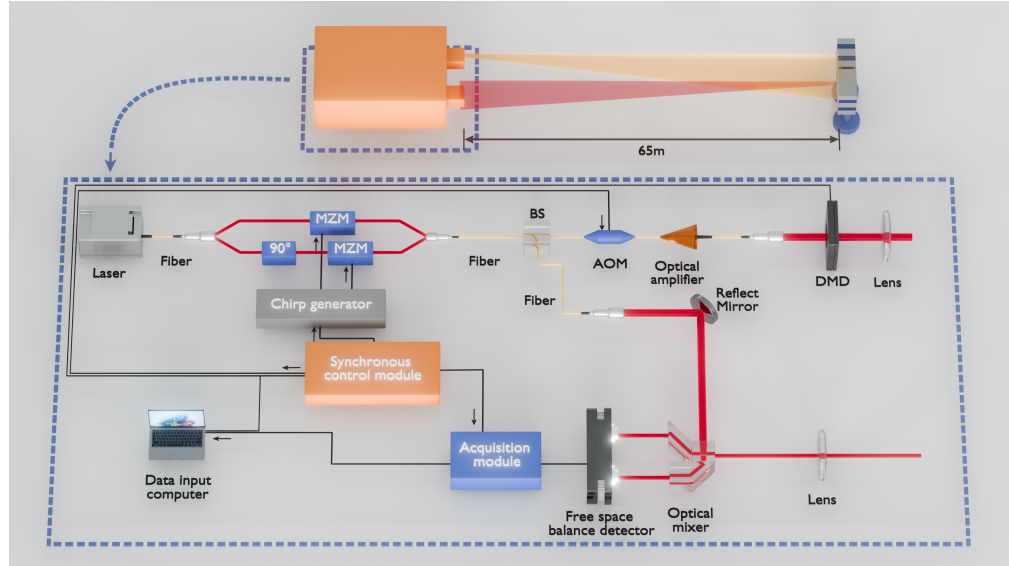


Fig. 2. Experimental setup of the bucket-detector-based multi-mode CD-GI lidar system.

After modulation, the temporal modulated light is divided by a fiber optic splitter (Thorlab,

TN1550R1A1, 99:1) into two paths. The weak branch (1%) is collimated using a fiber collimator (Thorlab, F260APC-1550) and used as the LO beam. The stronger branch (99%) is sent through an AOM (Qingjin-OE, G-1550-40-L-B-T-AA-A-Y-L), with a frequency offset of 40MHz, then amplified by an erbium-doped fiber amplifier (Shanghai Precilasers Technologies Co. Ltd.) and used as the object arm. The object arm is transmitted onto DMD (Texas Instruments, DLP-650-L-NIR) for spatial modulation through a fiber collimator(Thorlab, F260APC-1550), and then transmitted onto the target through a simple single-lens imaging system with a focal length of 800 mm and an aperture of 150 mm. Meanwhile, the light field reflected from the target is optically mixed with the LO beam in free space through the spatial optical mixer implemented in the imaging receiving system, which has a focal length of 250 mm and an aperture of 150 mm. The resulting IF signal is then obtained using a free-space balanced detector (Thorlabs, PDB230C).

3.1. Experiments of static target imaging in the bucket-detector-based multi-mode CD-GI lidar

In this configuration, the imaging lens of transmission in Fig. 2 yields a minimum resolvable feature size of approximately $1.22\lambda f/D \approx 10 \mu\text{m}$. The DMD has a resolution of 1280×800 and each micromirror has a size of $10.8\mu\text{m}$. The device operates at a refresh rate of 4 kHz. To match the resolution of imaging transmitting system, the minimum unit of Hadamard pattern is set to a 1-pixel binning, resulting in an encoded block size of $10.8 \mu\text{m}$. The effective coding region is 64×64 modulation array after binning. The imaging optical path is designed for the working distance of 65 m, and the magnification is calculated to be approximately $M = 80.25$, and the corresponding divergence angle is 0.85 mrad, corresponding to the FoV of 55.5 mm. The system has a fixed optical path offset of 7.2 m, originating from the internal fiber-optic path.

To investigate the imaging performance of the bucket-detector-based multi-mode CD-GI lidar under different surface scattering characteristics, experiments were conducted using both rough and smooth targets. The overall size of the targets was 55 mm. For the rough target, the object consisted of the four letters “SIOM”, where the letter were fabricated using a high-reflectivity film, while the background region was composed of low-reflectivity black cardboard. For the smooth target, the letter were made of black cardboard, and the background was a planar reflective mirror, forming a smooth reflective surface.

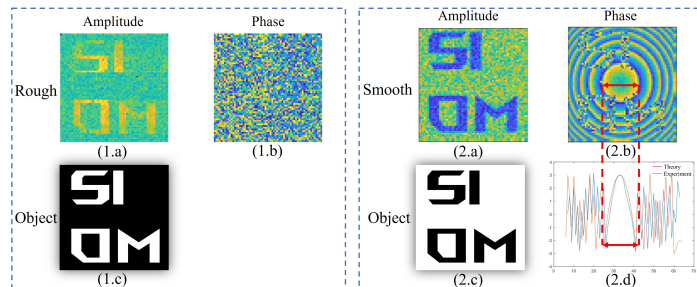


Fig. 3. The reconstructed image of amplitude and phase reconstructions for rough and smooth targets. (1.a) Amplitude and (1.b) phase images of the rough target, whose ground truth object is shown in (1.c). (2.a) Amplitude and (2.b) phase images of the smooth target, with the corresponding object shown in (2.c). The smooth target exhibits a clear deterministic phase distribution, whereas the rough target produces a spatially random phase. (2.d) One-dimensional phase profile extracted from the highlighted region in (2.b).

Fig. 3 presents a comparison of the reconstructed amplitude and phase images for rough and

smooth targets. For the rough target, the reconstructed amplitude image in Fig. 3(1.a) clearly reveals the “SIOM” pattern, whereas the corresponding phase image in Fig. 3(1.b) exhibits random fluctuations due to diffuse scattering from the rough surface. The ground-truth object is shown in Fig. 3(1.c) for reference.

In contrast, for the smooth target, both the amplitude image in Fig. 3(2.a) and the phase image in Fig. 3(2.b) show well-defined spatial structures. In particular, the phase image shows concentric fringe figures characteristic from a smooth surface. To further validate the phase reconstruction, Fig. 3(2.b) and Fig. 3(2.d) show that the experimental results agree well with $\exp\left[\frac{j\pi}{\lambda}\left(\frac{z_1+z_2}{z_2^2} + \frac{1}{z_3}\right) - \frac{z_2}{z_1} \rho_r\right]^2$ in the theoretical formula, which is caused by both the simple single-lens imaging system and the imaging receiving system.

Next, we experimentally investigate the IF signal energy and the energy of the reconstructed images in the bucket-detector-based multi-mode CD-GI lidar system.

3.2. Experiments of IF signal energy and reconstructed image energy in the bucket-detector-based multi-mode CD-GI lidar system

As shown in Eq. (11), to investigate the relationship among the imaging receiver aperture, detector area, and the IF signal energy, a series of black pinhole masks with diameters of 100 μm , 200 μm , and 300 μm (Edmund Optics) were sequentially placed on the detector plane to control the effective detection area. These pinhole diameters corresponded to FoV diameters of 25.9 mm, 51.8 mm, and 77.7 mm on the target plane at the working distance of 65 m. The target was a custom-fabricated circular structure with a diameter of 100 mm, ensuring uniform filling of the maximum effective detection area of the detector. The IF signal energy was obtained from repeated measurements of the first Hadamard pattern followed by ensemble averaging, while the reconstructed image energy was computed by converting the reconstructed intensity into corresponding energy values.

We confirmed a clear matching relationship between the receiver aperture and detector size that maximizes the IF signal energy, as shown in Fig. 4 (1.a)–(1.c). The horizontal axis represents the imaging receiver aperture, and the vertical axis represents the energy. Under single-mode LO conditions, the optimal receiver apertures for detectors with diameters of 300 μm , 200 μm , and 100 μm were measured to be 3.0 mm, 4.5 mm, and 9.5 mm, closely matching the theoretical predictions of 3.15 mm, 4.73 mm, and 9.46 mm. This result is in agreement with the effective mode field matching conditions predicted by the Siegman antenna theorem [56].

Moreover, we investigated the statistical characteristics of the IF signal energy in the bucket-detector-based multi-mode CD-GI lidar system and its relationship with the total energy of the reconstructed image pixels. The experimental results in Fig. 4 (2.a)–(2.b) show that the ratio of the total energy of all reconstructed image pixels to the coherent summation of the IF signal energy varies with detector size. Specifically, the measured ratios were 623.4 for $D_{\text{det}} = 300\mu\text{m}$ and 271.2 for $D_{\text{det}} = 200\mu\text{m}$. These ratios closely match the theoretical expectations based on the effective number of pixels shown in Eq. (12) (697 and 256, respectively, as detailed in Supplement 1, Sec. S4.A), directly validating the ability to decouple the coherence sum of the reflected multi-mode light fields to individual pixels using field correlation.

These two experimental results jointly demonstrate that, although the IF signal energy is constrained by Siegman antenna theorem [56], the exploitation of field correlation enables the reflected multi-mode light fields collected by the bucket detector to be coherently decoupled into effective single-mode components determined by the pixel size, thereby effectively circumventing the constraint imposed by Siegman antenna theorem.

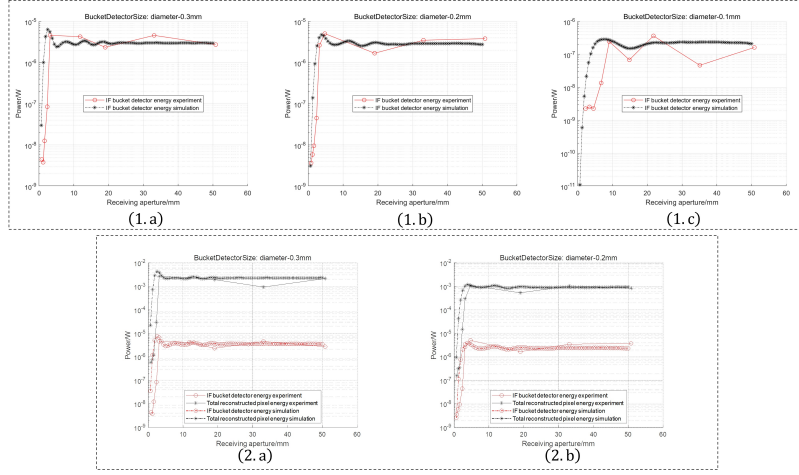


Fig. 4. IF signal energy and the total energy of all reconstructed pixels versus the receiving aperture variation range under different detector diameters (simulation and experiment). (1.a)-(1.c) Detector size: 300 μm , 200 μm , 100 μm . (2.a)-(2.b) Detector size: 300 μm , 200 μm .

3.3. Experiments of vibration modes

Building on these validations, the bucket-detector-based multi-mode CD-GI lidar is further applied in experiments to assess its capability in extracting target vibration modes.

3.3.1. Experiments of one vibrating target:

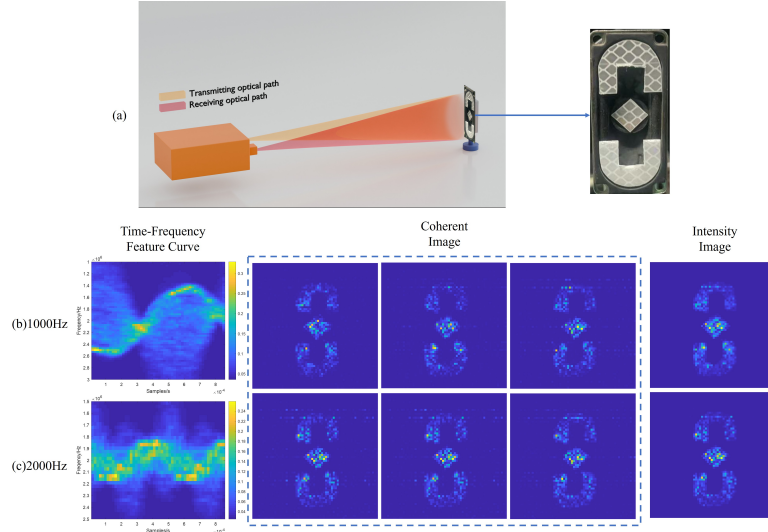


Fig. 5. Experimental results of spatial vibration mode reconstruction of the vibrating target: (a) simplified schematic of one vibrating target setup; (b) vibration frequency of 1000 Hz; (c) vibration frequency of 2000 Hz.

A loudspeaker (8 Ω , 5 W) was employed as the vibration source. Because the diaphragm material of the speaker has very low reflectivity at 1550 nm, a high-reflectivity (HR) film was

affixed to its surface to enhance the optical reflectivity. The target reflectivity distribution was set as Fig. 5 (a). The loudspeaker was driven by a sinusoidal voltage signal generated from a computer sound card, with vibration frequencies set to 1000 Hz and 2000 Hz. The DMD operated at an inversion repetition frequency of 1000 Hz.

Fig. 5 (b) and (c) display the vibration characteristics of the target at different excitation frequencies, including the time frequency spectrum of the vibration target, the reconstructed instantaneous coherent image at different time slices, and the superposed intensity image. Since the reconstructed vibration height are dynamic, they are provided as videos in the Supplementary Materials (Visualizations 1.1 and 1.2). These results demonstrate that the vibration mode of the target can be successfully reconstructed.

To investigate the changes in vibration modes at different driving frequencies, the target was configured as a strip-shaped object measuring 7 mm in width and 60 mm in length. The HR film was clamped at both ends, while the central region was adhered to a diaphragm using adhesive tape, forming a planar vibrating target. A simplified schematic of the experimental setup is shown in Fig. 6 (a). The vibration frequencies were set to 1000 Hz, 1500 Hz, and 2000 Hz. These frequencies were selected to assess the system's capability to detect and reconstruct micro-vibration characteristics across different temporal scales.

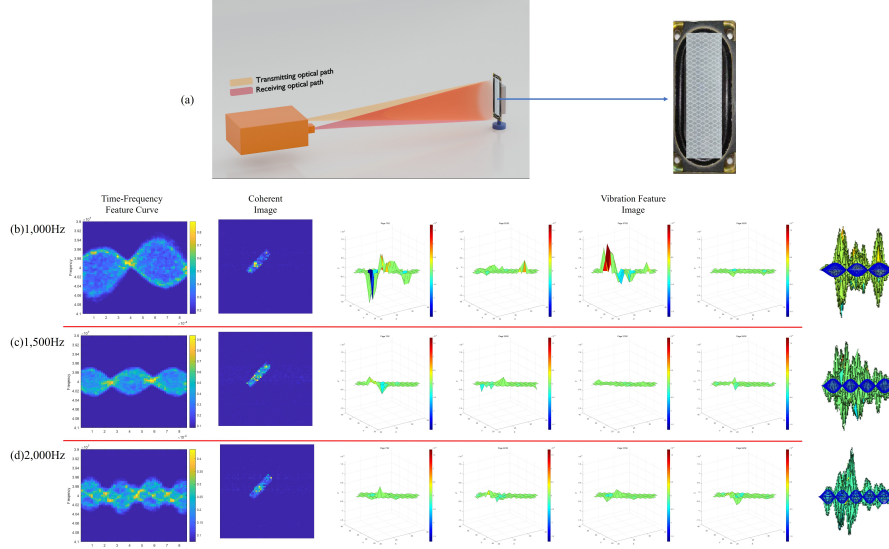


Fig. 6. Simplified schematic of the single vibrating target setup: (a), the vibrating feature information fusion diagram for one independent vibrating target, and each row corresponds to a different vibration frequency: (b)–(d) represent 1000 Hz, 1500 Hz, and 2000 Hz, respectively, from top to bottom. The coherent image shows the instantaneous intensity reflectivity image of the target reconstructed via field correlation. Then, the vibration feature image presents the vibration amplitude of the target at different vibration frequencies across uniformly spaced time slices. The last column shows the reconstructed longitudinal cross-sectional image of the vibration. The dark blue curve is the outer contour line of the vibration amplitude superimposed on each other.

According to the vibration modes reconstruction theory [57] for vibrating targets, Fig. 6 (b)–(d) illustrates the reconstructed vibrating feature information of the target at different vibration frequencies. The target vibrations at different frequencies are distinguishable in the time frequency spectrum of target. Under a fixed driving power, the amplitude of the target gradually decreases with increasing vibration frequency [58], which aligns with the physical behavior of a damped

driven harmonic oscillator. As the vibration frequency increases, more standing-wave nodes appear on the target surface, indicating that higher-order spatial vibration modes are excited by the external driving force. Since the reconstructed vibration height images are dynamic, we provide as a time-varying video in Visualizations 2.1, 2.2, and 2.3, representative frames are extracted at intervals of $66 \mu\text{s}$ based on the chosen time window length in the data processing.

3.3.2. The Imaging Experiment for Distinguishing Multiple Vibration Modes

To further evaluate the system's capability to simultaneously resolve multiple vibrating targets, a dual-target experiment was conducted. In this configuration, two strip-shaped vibrating targets with identical dimensions (7 mm in width and 60 mm in length) were positioned at different axial distances and independently driven at 500 Hz and 1000 Hz, respectively. The corresponding target distances were 65.00 m and 65.68 m. A simplified schematic of the experimental setup is shown in Fig. 7.

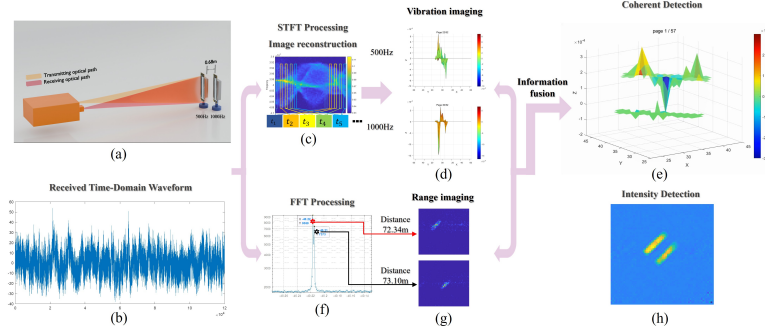


Fig. 7. Multidimensional information reconstruction results for dual vibrating targets: time-frequency information, complex reflectivity information, vibration mode information and distance information.(For the dynamic video, see Visualization 3). (a) Schematic of the experimental setup with transmitting and receiving optical paths. (b) Received time-domain waveform from the balanced bucket detector. (c) STFT processing and image reconstruction for different time slices. (d) Reconstructed vibration mode images corresponding to 500 Hz and 1000 Hz targets. (e) Coherent detection results showing the fusion information. (f) FFT processing of the time-domain waveform signal for range extraction. (g) Reconstructed range images for two targets at 72.34 m and 73.10 m. (h) Intensity detection results of the targets.

Fig. 7 presents the multidimensional information retrieved from the dual vibrating targets. First, feature extraction is performed on the time frequency spectrum obtained via STFT processing on Fig. 7 (c). By employing a curve-fitting approach, the vibration frequencies of the two targets are identified as 495 Hz and 1007 Hz. Next, based on temporal slicing, the vibration amplitude corresponding to each frequency component is calculated as shown in Fig. 7 (d), enabling the separation and reconstruction of the time-varying vibration mode maps of the two targets with distinct vibration frequencies. The dynamic evolution of the target vibration modes is provided in Visualization 3.

Then, pulse compression was applied to the electrical signal, which involves performing a FFT over the entire signal to extract the range information of the two targets as shown in Fig. 7 (f) and (g). The reconstructed target distances were 72.34 m (500 Hz) and 73.10 m (1000 Hz), yielding a longitudinal separation of 0.766 m. Compared with the actual separation of 0.680 m, the resulting deviation of 0.087 m falls well within the system's range resolution of $\Delta z = c/(2B) \approx 0.187 \text{ m}$, indicating reliable range discrimination. After determining the distance of each target, combining the range information with the reconstructed vibration modes allows for more precise target

characterization.

Finally, Fig. 7 (e) and (h) compare the target information reconstructed via intensity correlation and field correlation. Compared with intensity image, the proposed system enables simultaneous acquisition of target reflectivity, vibration frequency discrimination, and three-dimensional imaging.

4. Conclusion and Discussion

In summary, this work presents a CD-GI lidar strategy based on bucket detector of reflected multi-mode light fields. The system improves detection efficiency by employing a bucket detector. Meanwhile, the bucket-detector-based multi-mode CD-GI lidar system breaks the limitations of Siegman antenna theorem by exploiting field correlation to decouple the coherent summation of reflected multi-mode light fields. The results demonstrate that this strategy reconstructs the static spatial distribution of targets with high sensitivity under the spatiotemporal bandwidth product of a single detector and simultaneously retrieves their amplitude and phase information, enabling complex reflectivity imaging. In addition, this strategy not only discriminates targets according to their vibration frequencies, but also reconstructs the spatial distribution of targets' vibration modes. Moreover, the three-dimensional imaging capability is preserved, enabling a more comprehensive characterization of the target's spatiotemporal characteristics.

This work shows potential in applications such as autonomous sensing, non-contact structural health monitoring, precision micro-vibration measurement, and multi-modal remote sensing. By simultaneously acquiring time–frequency features and spatial vibration mode distributions, the system provides enriched target descriptors that enable more accurate recognition, classification, and comprehensive target analysis.

Funding. :

Acknowledgment. The authors would like to thank Professor Wenlin Gong for con-structive discussions.

Disclosures. The authors declare no conflicts of interest.

Data Availability Statement. Data underlying the results presented in this paper are not publicly available at this time but may be obtained from the authors upon reasonable request.

Supplemental document. See Supplement 1 and Visualization for supporting content.

References

1. J. H. Shapiro and R. W. Boyd, “The physics of ghost imaging,” *Quantum Inf. Process.* **11**, 949–993 (2012).
2. X. Qiu, H. Guo, and L. Chen, “Remote transport of high-dimensional orbital angular momentum states and ghost images via spatial-mode-engineered frequency conversion,” *Nat. Commun.* **14**, 8244 (2023).
3. Y. Zeng, Y. Li, W. Zhang, *et al.*, “Tailoring entanglement with a symmetry: Anomalous ghost diffraction,” *Phys. Rev. Appl.* **24**, 054002 (2025).
4. C. Zhao, W. Gong, M. Chen, *et al.*, “Ghost imaging lidar via sparsity constraints,” *Appl. Phys. Lett.* **101** (2012).
5. B. I. Erkmen, “Computational ghost imaging for remote sensing,” *J. Opt. Soc. Am. A* **29**, 782–789 (2012).
6. N. D. Hardy and J. H. Shapiro, “Computational ghost imaging versus imaging laser radar for three-dimensional imaging,” *Phys. Rev. A* **87**, 023820 (2013).
7. Y. Cheng, X. Zhou, X. Xu, *et al.*, “Radar coincidence imaging with stochastic frequency modulated array,” *IEEE J. Sel. Top. Signal Process.* **11**, 414–427 (2016).
8. X. Wang and Z. Lin, “Nonrandom microwave ghost imaging,” *IEEE Trans. on Geosci. Remote. Sens.* **56**, 4747–4764 (2018).
9. S. Sun, Z.-W. Nie, Y.-K. Xu, *et al.*, “Quantum-inspired computational wavefront shaping enables turbulence-resilient distributed aperture synthesis imaging,” *Sci. Adv.* **11**, eaea4152 (2025).
10. H. Yu, R. Lu, S. Han, *et al.*, “Fourier-transform ghost imaging with hard x rays,” *Phys. review letters* **117**, 113901 (2016).
11. S. Li, F. Cropp, K. Kabra, *et al.*, “Electron ghost imaging,” *Phys. review letters* **121**, 114801 (2018).
12. A. M. Kingston, G. R. Myers, D. Pelliccia, *et al.*, “Neutron ghost imaging,” *Phys. Rev. A* **101**, 053844 (2020).

13. Y.-H. He, Y.-Y. Huang, Z.-R. Zeng, *et al.*, “Single-pixel imaging with neutrons,” *Sci. Bull.* **66**, 133–138 (2021).
14. R. I. Khakimov, B. Henson, D. Shin, *et al.*, “Ghost imaging with atoms,” *Nature* **540**, 100–103 (2016).
15. Z. Liu, S. Tan, J. Wu, *et al.*, “Spectral camera based on ghost imaging via sparsity constraints,” *Sci. reports* **6**, 25718 (2016).
16. P. Wang, Z. Liu, J. Wu, *et al.*, “Dispersion control of broadband super-rayleigh speckles for snapshot spectral ghost imaging,” *Chin. Opt. Lett.* **20**, 091102 (2022).
17. L. Chen, P. Wang, Z. Liu, *et al.*, “Multicolor super-resolution structured illumination microscopy based on snapshot spectral ghost imaging via sparsity constraints,” *ACS Photonics* (2025).
18. P. Zhang, W. Gong, X. Shen, and S. Han, “Correlated imaging through atmospheric turbulence,” *Phys. Rev. A* **82**, 033817 (2010).
19. N. Hardy and J. Shapiro, “Reflective ghost imaging through turbulence,” *Phys. Rev. A* **84**, 063824 (2011).
20. W. Gong and S. Han, “Correlated imaging in scattering media,” *Opt. letters* **36**, 394–396 (2011).
21. M. Bina, D. Magatti, M. Molteni, *et al.*, “Backscattering differential ghost imaging in turbid media,” *Phys. review letters* **110**, 083901 (2013).
22. Y. Li, M. Chen, J. Qi, *et al.*, “Underwater ghost imaging with detection distance up to 9.3 attenuation lengths,” *Opt. Express* **31**, 38457–38474 (2023).
23. X. Zhang, J. Gao, Y. Gan, *et al.*, “Different channels to transmit information in scattering media,” *PhotonX* **4**, 10 (2023).
24. M. Bache, E. Brambilla, A. Gatti, and L. A. Lugiato, “Ghost imaging using homodyne detection,” *Phys. Rev. A* **70** (2004).
25. P. Zhang, W. Gong, X. Shen, *et al.*, “Homodyne detection in ghost imaging with thermal light,” *Phys. rev. a* **80**, 033827 (2009).
26. E. Ip and J. M. Kahn, “Coherent detection in optical fiber systems,” *Opt. Express* **16**, 753–791 (2008).
27. M. G. Taylor, “Phase estimation methods for optical coherent detection using digital signal processing,” *J. lightwave technology* **27**, 901–914 (2009).
28. K. Kikuchi, “Fundamentals of coherent optical fiber communications,” *J. lightwave technology* **34**, 157–179 (2015).
29. D. Fink, “Coherent detection signal-to-noise,” *Appl. Opt.* **14**, 689–690 (1975).
30. S. M. Beck, J. R. Buck, W. F. Buell, *et al.*, “Synthetic-aperture imaging laser radar: laboratory demonstration and signal processing,” *Appl. optics* **44**, 7621–7629 (2005).
31. L. Liu, X. Xiao, H. Guo, and D. Wang, “Coherent and incoherent synthetic-aperture imaging lidars,” *Appl. Opt.* **45**, 4879–4889 (2006).
32. C. J. Pellizzari, R. Trahan, H. Zhou, *et al.*, “Synthetic aperture lidar: A model-based approach,” *IEEE Trans. on Comput. Imaging* **3**, 901–916 (2017).
33. Z. W. Barber and J. R. Dahl, “Synthetic aperture lidar imaging demonstrations and information at very low return levels,” *Appl. optics* **53**, 5531–5537 (2014).
34. S. Wang, B. Wang, M. Xiang, *et al.*, “Synthetic aperture lidar motion compensation method based on symmetrical triangular linear frequency modulation continuous wave,” *Opt. Commun.* **471**, 125901 (2020).
35. P. F. McManamon, T. A. Dorschner, D. L. Corkum, *et al.*, “Optical phased array technology,” *Proc. IEEE* **84**, 268–298 (1996).
36. P. Gatt, T. P. Costello, D. A. Heimermann, *et al.*, “Coherent optical array receivers for the mitigation of atmospheric turbulence and speckle effects,” *Appl. optics* **35**, 5999–6009 (1996).
37. P. F. McManamon, P. J. Bos, M. J. Escutie, *et al.*, “A review of phased array steering for narrow-band electrooptical systems,” *Proc. IEEE* **97**, 1078–1096 (2009).
38. V. Dudorov, V. Aksenov, V. Kolosov, *et al.*, “Generation of vortex and partially coherent laser beams based on fiber array coherent combining,” in *Environmental Effects on Light Propagation and Adaptive Systems*, vol. 10787 (SPIE, 2018), pp. 88–94.
39. L. Liu, “Coherent and incoherent synthetic-aperture imaging lidars and laboratory-space experimental demonstrations,” *Appl. Opt.* **52**, 579–599 (2013).
40. C. V. Poulton, M. J. Byrd, P. Russo, *et al.*, “Coherent lidar with an 8,192-element optical phased array and driving laser,” *IEEE journal selected topics quantum electronics* **28**, 1–8 (2022).
41. B. Krause, P. Gatt, C. Embry, and J. Buck, “High-resolution 3d coherent laser radar imaging,” in *Laser Radar Technology and Applications XI*, vol. 6214 (SPIE, 2006), pp. 277–287.
42. M. L. Simpson, C. A. Bennett, M. S. Emery, *et al.*, “Coherent imaging with two-dimensional focal-plane arrays: design and applications,” *Appl. Opt.* **36**, 6913–6920 (1997).
43. H. Chen, M. S. Asif, A. C. Sankaranarayanan, and A. Veeraraghavan, “Fpa-cs: Focal plane array-based compressive imaging in short-wave infrared,” *arXiv preprint arXiv:1504.04085* (2015).
44. C. Deng, W. Gong, and S. Han, “Pulse-compression ghost imaging lidar via coherent detection,” *Opt. express* **24**, 25983–25994 (2016).
45. L. Pan, C. Deng, Z. Bo, *et al.*, “Experimental investigation of chirped amplitude modulation heterodyne ghost imaging,” *Opt. Express* **28**, 20808–20816 (2020).
46. D. C. Barton and J. D. Fieldhouse, “Noise, vibration and harshness (nvh),” in *Automotive chassis engineering*, (Springer, 2024), pp. 299–360.
47. V. Simonovskiy, I. Pavlenko, J. Pitel, *et al.*, “Methods and algorithms for calculating nonlinear oscillations of rotor

systems,” in *Design, Simulation, Manufacturing: The Innovation Exchange*, (Springer, 2021), pp. 63–74.

- 48. Y. Chai, W. Gao, B. AnKay, *et al.*, “Aeroelastic analysis and flutter control of wings and panels: a review,” *Int. J. Mech. Syst. Dyn.* **1**, 5–34 (2021).
- 49. M. Feldman, “Hilbert transform in vibration analysis,” *Mech. systems signal processing* **25**, 735–802 (2011).
- 50. V. Dekys, P. Kalman, P. Hanak, *et al.*, “Determination of vibration sources by using stft,” *Procedia Eng.* **177**, 496–501 (2017).
- 51. G. Manhertz and A. Bereczky, “Stft spectrogram based hybrid evaluation method for rotating machine transient vibration analysis,” *Mech. Syst. Signal Process.* **154**, 107583 (2021).
- 52. P. Ewert, B. Wicher, and T. Pajchrowski, “Application of the stft for detection of the rotor unbalance of a servo-drive system with an elastic interconnection,” *Electronics* **13**, 441 (2024).
- 53. Z. Huang and J. Liu, “Fast adaptive time-varying window length stft for compound track short-wave defects identification,” *J. Vib. Control.* **31**, 651–663 (2025).
- 54. Z. Zhong and S. Zhao, “Modified angular spectrum algorithm for the propagation of partially coherent beams in optical systems,” *J. Opt. Soc. Am. A* **40**, 741–746 (2023).
- 55. C. Song, J. He, and G. Yuan, “Generic full-vector angular spectrum method for calculating diffraction of arbitrary electromagnetic fields,” arXiv preprint arXiv:2505.13869 (2025).
- 56. A. Siegman, “The antenna properties of optical heterodyne receivers,” *Appl. optics* **5**, 1588–1594 (1966).
- 57. S. Liu, C. Deng, C. Wang, *et al.*, “Microvibration modes reconstruction based on micro-doppler coincidence imaging,” *IEEE Trans. on Geosci. Remote. Sens.* **60**, 1–16 (2022).
- 58. L. S. Jacobsen, “Steady forced vibration as influenced by damping: An approximate solution of the steady forced vibration of a system of one degree of freedom under the influence of various types of damping,” *Trans. Am. Soc. Mech. Eng.* **52**, 169–178 (1930).